Accurate low dimensional models for deterministic fluid systems driven by uncertain forcing

G. Dergham,[1,2] D. Sipp,[2] and J.-C. Robinet[1]
[1]*DynFluid Laboratory, Arts et Métiers ParisTech, 151 Bd de l'Hôpital, 75013 Paris, France*
[2]*Onera, Fundamental and Experimental Aerodynamics Department, 8 rue des vertugadins, 92190 Meudon, France*

(Received 20 October 2010; accepted 27 May 2011; published online 6 September 2011)

This paper addresses the model reduction of high-order linear systems within the framework of the incompressible Navier-Stokes equations. We look for reduced-order models that capture the response of some specific sensor whatever the initial flow condition and in the presence of any time-dependent external forcing. Namely, this work deals with the accurate modeling of the input-output dynamics of a fluid system when considering each degree of freedom of the system as an input, and the given measurement as the output. In the case of complex or realistic flows, the number of inputs is too large to apply the standard balanced truncation procedure. To alleviate this problem, we introduce a method called input projection. Input projection is shown to be analogous to the output projection procedure introduced by Rowley, Int. J. Bifurcation. Chaos Appl. Sci. Eng. **15**, 997 (2005). To illustrate the model reduction, we consider the dynamics of a globally stable flow over a rounded backward-facing step. Reduced-order models are obtained by projecting the full original system onto: (i) the basis of the leading balanced modes computed from the input-projected systems and (ii) the most observable modes. The balanced models are observed to accurately capture the transient growths along the separated flow whatever the input while outperforming the models based on the most observable modes. © *2011 American Institute of Physics*. [doi:10.1063/1.3622771]

I. INTRODUCTION

A variety of open flows, such as boundary layers, mixing layers, or separated flows, are subject to convective instabilities which amplify upstream low-level noise. In fact, even if globally stable, these flows may sustain large flow unsteadiness characterized by broadband frequencies due to the presence of permanent upstream noise.[1] These flows are often called selective noise-amplifiers and may be highly sensitive to small upstream perturbations (residual turbulence, noise, and surface roughness). In particular, the dynamics of such flows strongly depend on the characteristics of the upstream noise, which are unknown in practice. As a result, modeling the dynamics of amplifier flows remains a challenging task which, however, is crucial in many industrial applications. Typical examples are (i) the closed-loop control of the laminar-turbulent transition in boundary layer flows[2–4] and (ii) the design of near optimal state estimators in meteorology.[5,6] In both cases, due to the large size of the fluid systems, reduced-order models (ROMs) of the flow dynamics that capture the noise are required.

In order to capture such an unspecified noise, one solution consists of building ROMs which capture all the possible inputs. As a prototype example, we consider the flow over a rounded backward-facing step shown in Figure 1. This flow is assumed to be driven by an uncertain forcing at the upstream. Our objective is then to design low-order models that capture the linear dynamics on a single specific sensor, for all possible forcing configurations. Such a ROM may be very useful in the context of closed-loop control. For example, Bagheri *et al.*[2] assumed that the upstream noise was known in the design of their ROM. This noise was taken as a single spatial structure continuously forced in time by a white noise signal. The associated Linear Quadratic Gaussian (LQG) compensator will, therefore, only work for this specific spatial structure and location of the noise. Now, in real experiments, the noise is unknown and a model capturing all possible inputs would overcome this limitation.

A model reduction technique called balanced truncation is particularly suited for stable linear input-output systems.[7] It consists of finding a basis of equally controllable and observable modes ranked according to these properties. ROMs are obtained by the projection of the original system onto the leading balanced modes. Balanced truncation is said to be quasi-optimal to capture the dynamics from the inputs to the outputs since it offers theoretical bounds[8] on the transfer function error which are close to the lower bound achievable by any reduced-order model. This useful property makes it a very efficient and popular technique which brought the use of modern optimal flow control tools[9–13] within reach of current computational technology. Previous works on balanced truncation comprise the extension to nonlinear problems by Scherpen[14] and Lall *et al.*,[15] the introduction of an algorithm by Laub *et al.*[16] for the accurate and optimal computation of the balanced basis, and also the extension to unstable linear systems proposed by Zhou *et al.*[17]

Technically, the balanced basis can be computed as the eigenvectors of the product of two operators, namely the so-called controllability and observability Gramians.[18,19] For systems of moderate size, with up to $O(10^3)$ degrees of

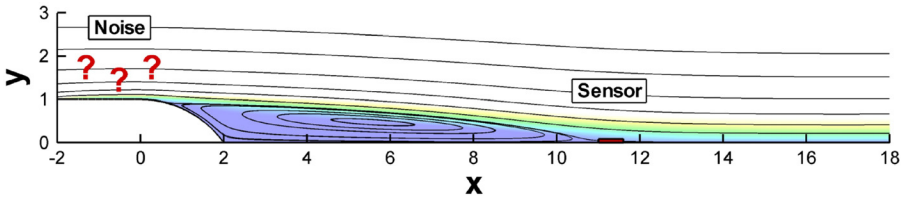

FIG. 1. (Color online) Backward-facing step flow investigated in this paper. The steady-state base flow at $Re = 600$ is depicted by its streamlines and longitudinal velocity. The upstream, downstream, and upper boundaries are, respectively, located at $x = -20$, $x = 100$, and $y = 20$. The exact position of the sensor is also displayed.

freedom, the balanced modes can be computed directly by computing explicitly the Gramians.[5,6,20,21] However, an approximate procedure is required for larger systems since this computation quickly becomes untractable. A recent extension proposed by Willcox and Peraire[22] and Rowley[23] has overcome this difficulty by approximating the balanced modes without computing the Gramians, by using a snapshot method. This technique, called balanced proper orthogonal decomposition (BPOD), has been performed on both stable[2,24,25] and unstable flow configurations.[26–28]

Balanced truncation designs efficient low order models which capture the dynamics from specific inputs to specific outputs. However, it may be completely ineffective to deal with the inputs and the outputs that have not been explicitly taken into account. In particular, it is not meant to model the true flow perturbation triggered from all the possible initial conditions unless both the input and the output spaces are chosen as the full state space. For large systems, using the method of snapshots requires the computation of one direct and one adjoint simulation per input and output. Consequently, choosing a large number of inputs and outputs quickly becomes unaffordable with the standard snapshot method. Though, Rowley[23] has introduced the technique called output projection to approximate the balanced modes for systems having a very large number of outputs. Output projection has been applied for the model reduction of a channel flow[24,29] and to perform closed-loop flow control on the flow past an inclined flat plate[26,28] by choosing the total kinetic energy of perturbations as the control objective to minimize.

Alternatively, another model reduction procedure is worth mentioning. The eigenvectors of the controllability and observability Gramians constitute two sets of orthogonal modes that may be considered to perform model reduction. The leading eigenmodes of the two Gramians account for the most controllable and observable states, respectively.[2] These modes have already been used to build reduced-order models for fluid systems.[2,23,24,27] In these cases, they are referred to as proper orthogonal decomposition (POD) models since they are computed from the classical method of snapshots introduced by Sirovich.[30] By construction, controllable modes optimally capture the energy triggered by the input while observable modes are the flow structures leading to maximum output energy. In spite of these properties, the resulting ROMs are known to be sub-optimal for capturing the input-output dynamics and may even be ineffective.[31]

In this paper, we are concerned with balanced truncation of stable linear input-output systems having a very large number of inputs. Particular attention is given to the case where the input is the full state, which stands for finding low order models that capture the dynamics from any initial condition or any forcing distribution to some given output. The procedure developed in this paper consists of an approximate balanced truncation and stands for an extension of the output projection procedure by Rowley.[23] In particular, the resulting ROMs are meant to quasi-optimally capture the input-output dynamics. Owing to its technical analogy with the output projection procedure, we call the present method input projection. The procedure is illustrated on the incompressible flow over a two-dimensional backward-facing step, which only accounts for a prototype of noise-amplifier flow. The formalism introduced here does not rely on physical insight into this particular flow configuration and can be applied to any other stable open flow configuration. The guideline of this paper is very similar to that adopted by Ilak and Rowley[24] where the performance of the output projection procedure is assessed on a channel flow. Notably, both the ROMs based on the most observable modes and the leading balanced modes are investigated. Their performance are evaluated and also compared. The goal of this paper is twofold: (i) show the ability of input projection to accurately model the "full-input to single output" transfer function of a large fluid system and (ii) to illustrate its quasi-optimality.

The rest of the paper proceeds along the following outline: in Sec. II, we start by introducing the model reduction procedures within the framework of the incompressible Navier-Stokes equations. These techniques are then applied to the two-dimensional flow over a backward-facing step, which is described in Sec. III. Results are presented in Sec. IV where the performance of the ROMs is assessed. A critical assessment of the input projection technique is provided in Sec. V and concluding remarks are presented in Sec. VI.

II. MODEL REDUCTION METHODOLOGY

A. Problem formulation

1. Governing equations

We consider the incompressible Navier-Stokes equations excited by a small noise (the input) together with a sensing (the output). The equations governing dynamics of the velocity $\boldsymbol{u}$ and pressure p fields are given by

$$\begin{cases} \partial_t \boldsymbol{u} + (\boldsymbol{u} \cdot \nabla)\boldsymbol{u} = -\nabla p + Re^{-1} \nabla^2 \boldsymbol{u} + \varepsilon \eta(t) \\ \nabla \cdot \boldsymbol{u} = 0 \\ m(t) = \mathcal{C}\boldsymbol{u} \end{cases}, \qquad (2.1)$$

where Re denotes the Reynolds number and $\eta(t)$ stands for a field modeling the noise. The parameter ε points out that the

noise is small compared to the other terms of the equation. Thus, $\epsilon\eta(t)$ acts as a small time dependent forcing on the momentum equation. As in a practical case, we consider that the spatial and temporal distributions of the noise $\eta(t)$ are unknown. Since the velocity field has a divergence-free constraint, it can easily be shown that only the divergence-free part of $\eta(t)$ will have an effect on the system, so that we can suppose that $\nabla\cdot\eta(t)=0$. This forcing term $\eta(t)$ is considered as the input of our problem in the following.

The measure denoted by $m(t)$ represents a quantity extracted from the flow by some sensors. Mathematically, it is expressed as the result of a measure operator $\mathcal{C}$ applied to the velocity field $\boldsymbol{u}$. For simplicity, we will consider in this work a single sensor, so that $m(t)$ is a scalar. This measurement is also referred to as the output of our system. In this context, we wish to design ROMs capable of capturing the linear input-output dynamics of this system. In other words, we wish to model accurately these dynamics whatever the noise distribution.

First, we linearize the dynamics given by Eq. (2.1) at the order ε about a base flow. This base flow is chosen here to be the solution of the associated steady Navier-Stokes equations with $\varepsilon=0$. The velocity of the base flow is denoted by $\boldsymbol{U}$ in the following and we adopt, for simplicity, the notation $(\boldsymbol{u},p)$ for the perturbation field and $m(t)$ for the measure of the perturbation. The resulting set of equations reads

$$\begin{cases} \partial_t\boldsymbol{u}+\boldsymbol{U}\cdot\nabla\boldsymbol{u}+\boldsymbol{u}\cdot\nabla\boldsymbol{U}=-\nabla p+Re^{-1}\nabla^2\boldsymbol{u}+\eta(t) \\ \nabla\cdot\boldsymbol{u}=0 \\ m(t)=\mathcal{C}\boldsymbol{u} \end{cases}, \tag{2.2}$$

which accounts for the linear dynamics of the perturbations about the base flow. Within a numerical approach, Eq. (2.2) are discretized on a mesh. It can be shown (see Appendix A) that we can write the resulting discretized equations in the following matrix form

$$\frac{d\mathsf{X}}{dt}=\mathsf{A}\mathsf{X}+\eta(t), \tag{2.3a}$$

$$m(t)=\mathsf{C}\mathsf{X}, \tag{2.3b}$$

where X and C denote the vectors resulting from the discretization of $\boldsymbol{u}$ and $\mathcal{C}$. Additionally, we assumed that $\eta(t)$ and $m(t)$ maintain the same notation once discretized, and the matrix A represents the linearized Navier-Stokes operator which is supposed to be stable in the following. Equations (2.3) constitute the stable linear input-output state-space system considered in the following. The size of this system, denoted by n, is also its number of degrees of freedom. Thus, the matrix A is of size $n\times n$, the states X and $\eta(t)$ are of size $n\times 1$ and C is of size $1\times n$.

2. Definition of the norms

Mathematically, there are two relevant and equivalent quantities for assessing the input-output behavior of system (2.3): the impulse response $g(t)=\mathsf{C}e^{\mathsf{A}t}$ and the transfer function $\mathsf{G}(\omega)=\mathsf{C}(i\omega\mathsf{I}-\mathsf{A})^{-1}$. To quantify the performance of the ROMs, we compute the error on the transfer function, which requires the definition of some norms.

First, let us introduce an inner product, denoted by $\langle\rangle$, on the state space. This inner product is chosen as the standard energy inner product. It is defined for two states Z_1 and Z_2, corresponding to the velocities $\boldsymbol{u}_1$ and $\boldsymbol{u}_2$, by

$$\langle\mathsf{Z}_1,\mathsf{Z}_2\rangle=\int_\Omega \boldsymbol{u}_1\cdot\boldsymbol{u}_2\,d\Omega, \tag{2.4}$$

where Ω is the fluid volume. We also suppose that the input space, which is equal to the state space, is endowed with the same inner product. It is then possible to define the adjoint operator $\mathsf{A}^\dagger$ by

$$\langle\mathsf{Z}_1,\mathsf{A}\mathsf{Z}_2\rangle=\langle\mathsf{A}^\dagger\mathsf{Z}_1,\mathsf{Z}_2\rangle, \tag{2.5}$$

for all possible states Z_1 and Z_2. Furthermore, we define the adjoint of the state X and of the operator C by

$$\langle\mathsf{X},\mathsf{Z}\rangle=\mathsf{X}^\dagger\mathsf{Z}\quad\text{and}\quad\mathsf{C}\mathsf{Z}=\langle\mathsf{C}^\dagger,\mathsf{Z}\rangle, \tag{2.6}$$

for all possible states Z. Note that $g(t)$ and $\mathsf{G}(\omega)$ are vectors of size $1\times n$; their adjoint are defined similarly to that of C. It is straightforward to show that $\mathsf{G}^\dagger(\omega)=(-i\omega\mathsf{I}-\mathsf{A}^\dagger)^{-1}\mathsf{C}^\dagger$ and $g^\dagger(t)=e^{\mathsf{A}^\dagger t}\mathsf{C}^\dagger$, which are both of size $n\times 1$.

The norm associated with the inner product $\langle\rangle$ will be denoted by $||\ ||$ in the following. It is defined for a state X by $||\mathsf{X}||=\sqrt{\langle\mathsf{X},\mathsf{X}\rangle}$. From this inner product, it is possible to define two standard norms to quantify the transfer function. The 2-norm of the transfer function G is defined by either a frequency or a time integral

$$||\mathsf{G}||_2=\sqrt{\frac{1}{2\pi}\int_{-\infty}^{+\infty}||\mathsf{G}^\dagger(\omega)||^2d\omega}=\sqrt{\int_0^{+\infty}||\mathsf{g}^\dagger(t)||^2dt}. \tag{2.7}$$

Furthermore, we also consider the ∞-norm of the transfer function which is defined by

$$||\mathsf{G}||_\infty=\max_\omega||\mathsf{G}^\dagger(\omega)||. \tag{2.8}$$

Note that both norms are satisfactorily defined since we assumed that A is stable. In addition, the two norms $||\ ||_2$ and $||\ ||_\infty$ should not be confused with the norm $||\ ||$ that measures a state.

B. Balanced truncation

Balanced truncation is a well-known model reduction technique used for stable linear input-output systems. It relies on the concept of controllability and observability of the flow states. Controllability quantifies how easy a state can be reached from any other state, while observability quantifies the amount of measure triggered by a given flow state.[7] The key idea of balanced truncation is to find a basis of equally controllable and observable modes and project the original equations onto the set of the most controllable/

observable modes. This basis, which is called the balanced basis, may be computed[7] as the eigenvectors of the product of the controllability and observability Gramians defined, respectively, by

$$\mathsf{G}_c = \int_0^{+\infty} e^{\mathsf{A}t} e^{\mathsf{A}^\dagger t} dt \qquad \mathsf{G}_o = \int_0^{+\infty} e^{\mathsf{A}^\dagger t} \mathsf{C}^\dagger \mathsf{C} e^{\mathsf{A}t} dt. \tag{2.9}$$

For large systems, a procedure known as BPOD (Ref. 23) yields a snapshot-based approach to approximate balanced truncation. It relies on the computation of the matrices $\mathsf{X}(t) = e^{\mathsf{A}t}$ and $\mathsf{Y}(t) = e^{\mathsf{A}^\dagger t}\mathsf{C}^\dagger$ for a discrete set of times in order to stack them (with appropriate quadrature weights) as columns of the matrices $\mathbf{X}$ and $\mathbf{Y}$ such that the Gramians may be factored as

$$\mathsf{G}_c \approx \mathbf{X}\mathbf{X}^\dagger \qquad \mathsf{G}_o \approx \mathbf{Y}\mathbf{Y}^\dagger. \tag{2.10}$$

Next, one can compute the balanced basis from the singular value decomposition $\mathbf{Y}^\dagger\mathbf{X} = \mathsf{M}\Sigma\mathsf{N}^*$, where * denotes the transconjugate. The balanced basis T and its inverse S are found by

$$\mathsf{T} = \mathbf{X}\mathsf{N}\Sigma^{-1/2} \qquad \mathsf{S} = \mathbf{Y}\mathsf{M}\Sigma^{-1/2}, \tag{2.11}$$

where the balanced modes are the columns of the matrix T while its biorthogonal basis constitutes the columns of S. Note that their orthogonality relation reads $\mathsf{S}^\dagger\mathsf{T} = \mathsf{I}$. The entries of the diagonal matrix Σ are known as the Hankel singular values (HSVs) and refer to the equal controllability and observability of the associated balanced modes.

Using the snapshot method introduced by Rowley,[23] the computation of $\mathsf{Y}(\mathsf{t}) = e^{\mathsf{A}^\dagger t}\mathsf{C}^\dagger$ requires one adjoint simulation since there is only one output. However, the computation of $\mathsf{X}(t) = e^{\mathsf{A}t}$ is not tractable since it would require n direct simulations, one for each degree of freedom of the system. The computation of the exact balanced basis associated with system (2.3) is thus not possible in our case. Yet, we alleviate this problem by considering instead (i) the observable modes, which are already known in the literature and (ii) the balanced modes computed by using the technique introduced in this paper and called "input projection."

C. Observable modes

First, we consider an orthogonal basis of modes ranked according to their observability. These modes are obtained as the leading eigenvectors of the observability Gramian G_o. The resulting flow structures are by definition the most observable states and are ranked according to their contribution to the output energy.[2]

For large systems, the leading observable modes can be computed by using the standard snapshot method.[23] The first step is to compute the flow states $\{\mathsf{Y}(t) = e^{\mathsf{A}^\dagger t}\mathsf{C}^\dagger;\ t > 0\}$ with an adjoint simulation to build the matrix $\mathbf{Y}$. Next, we compute the singular value decomposition $\mathbf{Y}^\dagger\mathbf{Y} = \mathsf{L}\Lambda\mathsf{L}^*$. The leading observable modes are then obtained as the columns of the matrix R given by

$$\mathsf{R} = \mathbf{Y}\mathsf{L}\Lambda^{-1/2}. \tag{2.12}$$

Note that the orthogonality of these modes reads $\mathsf{R}^\dagger\mathsf{R} = \mathsf{I}$. It should also be noticed that the observable modes reduce to the POD modes of the dataset $\{\mathsf{Y}(t);\ t > 0\}$ computed with the energy inner product. The diagonal matrix Λ yields the leading eigenvalues of G_o which account for the observability of the corresponding eigenvectors.

Reduced-order models can then be obtained by projecting the full system (2.3) onto the most observable modes. The choice of such ROMs is intuitively motivated insofar as it is based on the modes having the highest contribution to the sensor energy. However, contrary to balanced models, these ROMs are sub-optimal (and may be ineffective) in capturing the true input-output dynamics.

D. Input projection

The second approach considered here is the method called input projection. The idea is to project the input $\eta(t)$ on a low-dimensional subspace while optimally preserving, in the 2-norm sense, the original transfer function. If we introduce an orthogonal projection P_s on a s-dimensional subspace of the input space, the new input-output system reduces to

$$\frac{d\mathsf{X}}{dt} = \mathsf{A}\mathsf{X} + \mathsf{P}_s\eta(t), \tag{2.13a}$$

$$\tilde{m}(t) = \mathsf{C}\mathsf{X}, \tag{2.13b}$$

where $\tilde{m}(t)$ is the output of the input-projected system. We look for the projection P_s that minimizes the 2-norm error between the original impulse response $\mathsf{G}(\omega)$ and that of the input-projected system, which is given by $\tilde{\mathsf{G}}(\omega) = \mathsf{G}(\omega)\mathsf{P}_s$. This error can be expressed by

$$||\mathsf{G} - \mathsf{G}\mathsf{P}_s||_2 = \sqrt{\int_0^{+\infty} ||\mathsf{g}^\dagger(t) - \mathsf{P}_s\mathsf{g}^\dagger(t)||^2 dt}, \tag{2.14}$$

since $\mathsf{P}_s^\dagger = \mathsf{P}_s$. Furthermore, noting that $g^\dagger(t) = \mathsf{Y}(t)$, we infer that the projection that minimizes this error stands for the projection onto the first s POD modes of the dataset $\{\mathsf{Y}(t);\ t > 0\}$. In other words, P_s reduces to the orthogonal projection onto the most observable modes which were introduced in Sec. II C. Consequently, P_s can be written as

$$\mathsf{P}_s = \mathsf{R}\mathsf{R}^\dagger, \tag{2.15}$$

where R is the matrix of size $n \times s$ whose columns are the first s observable modes. Thus P_s is a matrix of size $n \times n$ and of rank s.

By construction, only the s most important degrees of freedom of the input $\eta(t)$ have an effect on the output $\tilde{m}(t)$. By considering $\tilde{\eta}(t) = \mathsf{R}^\dagger\eta(t)$ as a new input of size $s \times 1$, the system (2.13) can then be written as

$$\frac{d\mathsf{X}}{dt} = \mathsf{A}\mathsf{X} + \mathsf{R}\tilde{\eta}(t), \tag{2.16a}$$

$$\tilde{m}(t) = \mathsf{C}\mathsf{X}. \tag{2.16b}$$

This new input-output system possesses the same controllability and observability Gramians as those of system (2.13).

It is referred to as the s input-projected system hereafter. Interestingly, the computation of the balanced modes of this new system becomes affordable since it only requires s direct simulations, one for each column of R to get $\mathsf{X}(t)=e^{\mathsf{A}t}\mathsf{R}$. The balanced basis of system (2.16) will be denoted by T and S in the rest of the paper. It should also be emphasized that these balanced modes depend on the parameter s and that they approximate the balanced modes of the original system (2.3).

Note that the idea to project the input state is analogous to the method called output projection introduced by Rowley[23] and performed by Ilak and Rowley[24] and Ahuja and Rowley.[28] In their case, the output of the system is the entire state space so that they optimally project the output on a low-dimensional subspace. In fact, the input projection introduced here can be interpreted as the output projection on an adjoint system. This observation is presented in more detail in Appendix C.

E. Model reduction

Reduced-order models are obtained by projecting the input-projected equations (2.13) onto the basis of its leading balanced modes. Keeping the first r balanced modes (columns of T and S) the dynamics of the reduced state X_r, which is of size $r\times 1$, are given by

$$\frac{d\mathsf{X}_r}{dt}=\mathsf{A}_r\mathsf{X}_r+\mathsf{B}_r\eta(t), \tag{2.17a}$$

$$\tilde{m}_r(t)=\mathsf{C}_r\mathsf{X}_r, \tag{2.17b}$$

where $\tilde{m}_r(t)$ is the output of the reduced-order model and the above-introduced matrices are defined by

$$\begin{array}{lll}\mathsf{X}_r=\mathsf{S}^\dagger\mathsf{X} & \mathsf{A}_r=\mathsf{S}^\dagger\mathsf{A}\mathsf{T} & \mathsf{B}_r=\mathsf{S}^\dagger\mathsf{P}_s\\ \mathsf{C}_r=\mathsf{C}\mathsf{T}, & & \end{array} \tag{2.18}$$

where A_r is of size $r\times r$, B_r is of size $r\times n$, and C_r is of size $1\times r$. The corresponding transfer function is then defined by $\tilde{\mathsf{G}}_r(\omega)=\mathsf{C}_r(i\omega\mathsf{I}_r-\mathsf{A}_r)^{-1}\mathsf{B}_r$, where I_r stands for the identity matrix of size r.

ROMs based on the most observable modes are also considered in the following. These models are obtained by using the same procedure by replacing T and S by R.

III. APPLICATION TO A BACKWARD-FACING STEP FLOW

A. Flow configuration

1. Geometry

We consider a two-dimensional rounded backward facing step of circular geometry, see Figure 1, and an incoming flow from the left. This geometry was originally studied by Duriez.[32] The upstream velocity and the step height are used to make all quantities non-dimensional. The beginning and end of the step are located at $(x=0,\ y=1)$ and $(x=2,\ y=0)$, respectively. The boundary conditions are the following: (i) a uniform and unitary velocity field $(u=1,\ v=0)$ is prescribed at the inlet boundary $x=-20$. (ii) A free-slip condition with zero tangential stress $(\partial_y u=0,\ v=0)$ is prescribed on the boundary $(-20\le x\le -2,\ y=1)$. (iii) A laminar boundary layer starts developing on the lower boundary at $x=-2$ as no-slip boundary conditions $(\boldsymbol{u}=0)$ are imposed on $(-2\le x\le 0,\ y=1)$, on the step wall, and on the downstream wall $(2\le x\le 100,\ y=0)$. (iv) Symmetry boundary conditions are used at the upper boundary $y=20$, and (v) a free outflow condition $p\boldsymbol{n}-Re^{-1}(\nabla\boldsymbol{u})\cdot\boldsymbol{n}=0$ is used at the outlet $x=100$ ($\boldsymbol{n}$ being the outward normal unitary vector of the boundary).

2. Problem discretization

We used a finite element approach to discretize the problem. The variational formulation of the governing equations is spatially discretized using a mesh composed of triangular elements. The velocity fields are projected onto six-node quadratic triangular elements with quadratic interpolation (P2-elements), whereas the pressure field is discretized using three-node linear triangular elements (P1-elements). The matrices resulting from the projection of the variational formulations onto the basis of finite elements are sparse and are built with the FreeFem++ software (http://www.freefem.org). The mesh considered in this work yields $n\approx 360\,000$ degrees of freedom stemming from about 90 000 triangles.

3. Base flow

The base flow considered here is computed by using a Newton-Raphson method[33] for a Reynolds number $Re=600$. The solution is depicted in Figure 1. At this Reynolds number, the flow is observed to be globally stable; the matrix A does not have any unstable eigenvalues. The displacement thickness at $x=0$ is $\delta^*\approx 0.082$, leading to a Reynolds number based on the displacement thickness of $Re_{\delta}*\approx 49.2$. The boundary layer separates at $x\approx 0.6$ and reattaches at $x\approx 11$. Even if this base flow is globally stable, it may sustain flow unsteadiness due to the transient energy growth of perturbations. The Kelvin-Helmholtz instability selectively amplifies the upstream low-level noise along the shear layer to drive the flow dynamics downstream. As shown in Figure 1 by the question-marks, the noise distribution is assumed to be unknown. The sensor is placed downstream in the vicinity of the reattachment point. The measured quantity is chosen as the wall-normal shear stress evaluated at and integrated over a localized region of the wall, namely $m(t)=\int_{x=11}^{x=11.6}\partial_y u\,dx$. This choice of measurement also defines the output operator C.

B. Computation of the modes

The balanced and observable modes are computed from the singular value decomposition of $\mathbf{Y}^\dagger\mathbf{X}$ and $\mathbf{Y}^\dagger\mathbf{Y}$, respectively. The computation of the matrices $\mathbf{X}$ and $\mathbf{Y}$ is based on the frequential expressions of the Gramians[22] derived from the Parseval's theorem

$$\begin{cases}\mathsf{G}_c=\frac{1}{2\pi}\int_{-\infty}^{+\infty}(j\omega\mathsf{I}-\mathsf{A})^{-1}\mathsf{R}\mathsf{R}^\dagger(-j\omega\mathsf{I}-\mathsf{A}^\dagger)^{-1}d\omega\\ \mathsf{G}_o=\frac{1}{2\pi}\int_{-\infty}^{+\infty}(-j\omega\mathsf{I}-\mathsf{A}^\dagger)^{-1}\mathsf{C}^\dagger\mathsf{C}(j\omega\mathsf{I}-\mathsf{A})^{-1}d\omega\end{cases}. \tag{3.1}$$

By considering these expressions, we compute the matrices $\widehat{\mathsf{X}}(\omega) = (j\omega\mathsf{I} - \mathsf{A})^{-1}\mathsf{R}$ and $\widehat{\mathsf{Y}}(\omega) = (-j\omega\mathsf{I} - \mathsf{A}^{\dagger})^{-1}\mathsf{C}^{\dagger}$ for a discrete set of frequencies in order to stack them as the columns of the matrices **X** and **Y**. To this end, we used 399 equidistant frequencies ranging from $\omega = 0$ to $\omega = 4$ and quadrature coefficients corresponding to the 4th-order Simpson method. This choice proved to be sufficient for an accurate computation since for a larger number of snapshots with a finer spacing or a larger frequency interval, there is no considerable change in the singular values and modes considered here. For each frequency, $\widehat{\mathsf{Y}}(\omega)$ is computed by one matrix inversion since $\mathsf{C}^{\dagger}$ is a vector. Likewise, s inversions are required to get $\widehat{\mathsf{X}}(\omega)$, one for each column of R. These matrix inversions are performed through a direct multifrontal sparse LU solver (MUltifrontal Massively Parallel sparse direct Solver (MUMPS) (Ref. 34)). Further details on the discretized formulation of the Gramians resulting from our choice of inner product are available in Appendix B.

It should be mentioned that the temporal expressions of the Gramians are usually adopted to factor the Gramians in Eq. (2.10).[2,24,27,28] The present frequential approach has been proved to be equivalent to the temporal one[17,22] and it has been applied to the same backward-facing step flow configuration by Dergham *et al.*[25] Whether using the temporal or the frequential approach leads in the end to the same projection basis and to the same ROMs; one may simply choose between the two according to the available computational tools.[25]

IV. RESULTS

A. Observable modes

Using the procedure outlined in Sec. II C, we compute the most observable modes by using Eq. (2.12). The singular values λ_j, ranking the observability of associated states, are represented in Figure 2(a). The observability of the modes is seen to fall-off quite rapidly indicating that only the first modes will have a significant contribution to the measured energy. We have represented in Figures 2(b)–2(e) the first, second, third, and 12th observable modes, visualized by their streamwise velocity component. The first eigenvalues are in pairs, indicating that the most significant modes are traveling

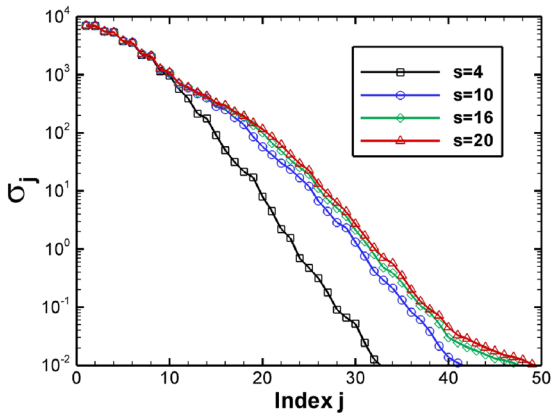

FIG. 3. (Color online) First 50 HSVs σ_j corresponding to the input-projected systems $s = 4,10,16,20$.

structures that are 90° out of phase, Figures 2(b) and 2(c) illustrate this statement.

As one could expect, the flow structures which yield a maximum energy on the sensor are located upstream. The first modes are spatially located in the vicinity of the separation point while higher modes, as the 12th, have a more extended spatial support. These most observable structures are tilted in the upstream direction, leaning against the shear layer. This result is consistent with other recent works[2,35] where it is interpreted as a way to extract energy from the mean shear by transporting momentum down the velocity gradient[36] by the so-called Orr mechanism. For the sake of simplicity, the ROMs obtained by projection onto the most observable modes are referred to as "observable models" in the following.

B. Balanced modes

Next, we compute the balanced modes of the input-projected system (2.16). Several values of the rank s of input-projection, ranging from 1 to 20, have been considered. The balanced basis (T;S) and its associated HSVs σ_j depend on this rank. Figure 3 depicts the HSVs of input projected systems of rank 4, 10, 16, and 20. It is observed that increasing the rank of input projection leads to a convergence of the leading HSVs. In addition, the number of converged HSVs

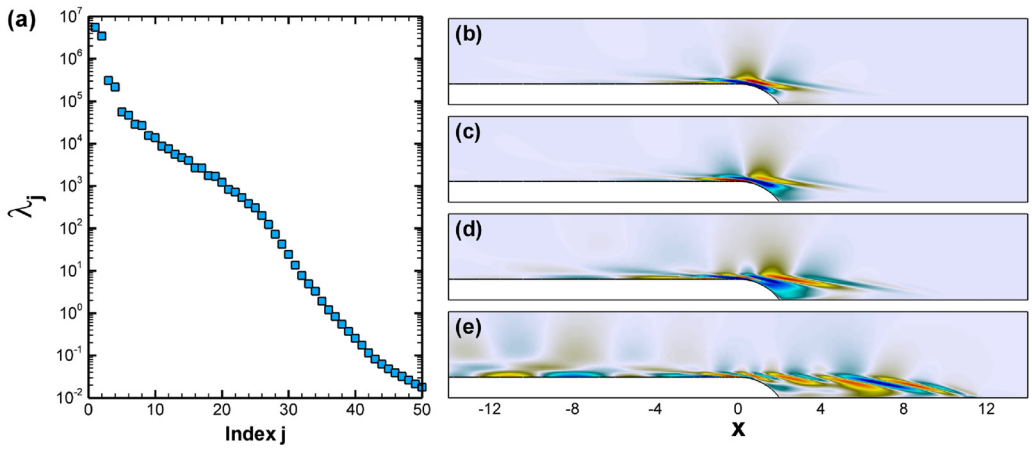

FIG. 2. (Color online) (a) First 50 observable eigenvalues λ_j. Figures (b)–(e) represent the longitudinal velocity of the first, second, third, and 12th observable modes.

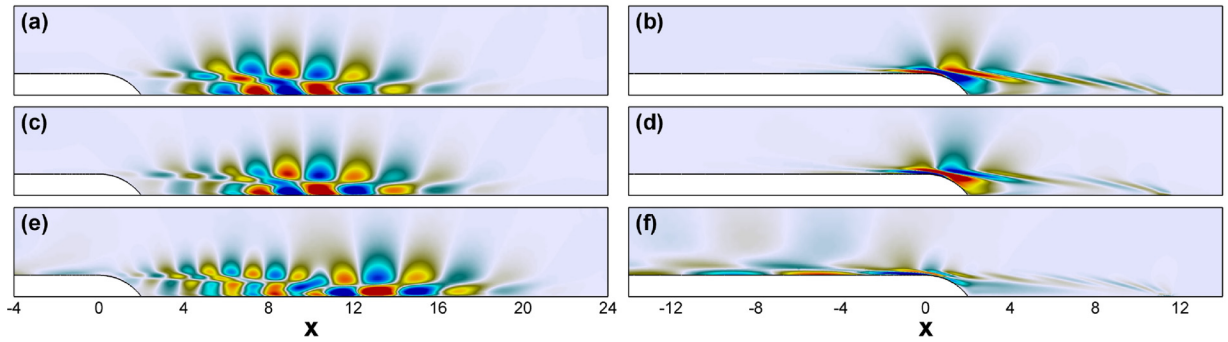

FIG. 4. (Color online) Figures (a) and (b) represent the longitudinal velocity of the first balanced mode and its adjoint, respectively. (c) and (d) depict analogously the third modes while (e) and (f) represent the 12th. These modes have been computed from an input-projected system with $s = 20$.

for each input projection is approximately equal to the input-projection rank s, which was also noticed in previous works using the output projection procedure.[23,24,28] It should be emphasized that this convergence is also noted for the associated leading balanced modes (not shown here). The first Hankel singular values also come in pairs, indicating that the most significant balanced modes are traveling structures. The HSVs, assessing the controllability/observability of associated states are also observed to fall-off quite rapidly, indicating that only the first modes will have a significant contribution to the overall input-output behavior.

We have represented in Figures 4(a)–4(f) the first, third, and 12th balanced modes computed for the case $s = 20$. Figures 4(a), 4(c), and 4(e) depict the balanced modes (columns of T) while Figures 4(b), 4(d), and 4(f) stand for their associated adjoint (columns of S). We observe that the leading balanced modes appear as wavepackets that are somewhat more spatially extended than the observable modes. We also note a spatial separation between the balanced modes and their adjoint. Essentially, this separation highlights the non-orthogonality of the balanced modes. This point can be interpreted[2,24] as a consequence of the convective nature of the instabilities along the shear layer in which disturbances grow in amplitude as they are convected in the downstream direction.[37,38] As a result, the controllable and observable subspaces are separated in the streamwise direction which implies that the distribution of both the input (the full state) and the output (the sensor) may hardly be captured by an orthogonal projection onto the leading modes of only one subspace. The ROMs resulting from the projection onto the leading balanced modes are called the "balanced models" hereafter.

C. Performance of the ROMs

The leading observable and balanced modes are used to build reduced-order models. Their performance in capturing the original dynamics of the full system (2.3) is assessed by scrutinizing how the input-output transfer function is captured. To that purpose, we compute the relative errors of the reduced transfer functions. Both the 2-norm and the ∞-norm have been considered. Their associated relative errors are denoted by e_2 and e_∞, respectively. They are defined for a model of size r by

$$e_2(r) = \frac{||\mathsf{G} - \widetilde{\mathsf{G}}_r||_2}{||\mathsf{G}||_2} \qquad e_\infty(r) = \frac{||\mathsf{G} - \widetilde{\mathsf{G}}_r||_\infty}{||\mathsf{G}||_\infty}, \tag{4.1}$$

where the full transfer function is computed from the snapshots $\widehat{\mathsf{Y}}(\omega)$ by $\mathsf{G}(\omega) = \widehat{\mathsf{Y}}^{\dagger}(\omega)$, see Appendix B3. The evolution of these two errors with the size of the ROMs is presented in Figures 5(a) and 5(b), respectively. Both yield a

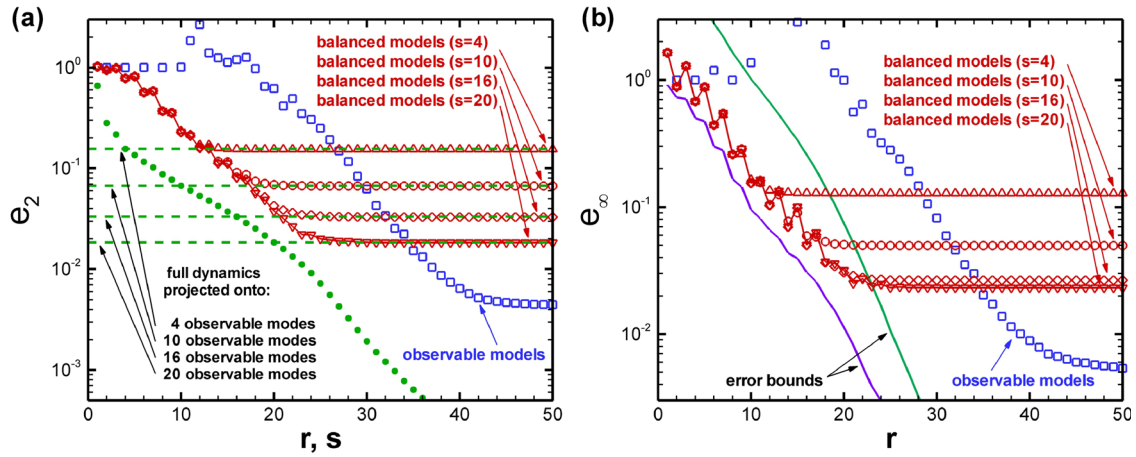

FIG. 5. (Color online) Relative error norm of observable and balanced models as a function of their size r. (a) represents the 2-norm while (b) accounts for the ∞-norm. The 2-norm error limits due to input projection are depicted on (a) as a function of the projection rank s by dots. The dashed lines illustrate these error limits for the ranks $s = 4,10,16,20$. The ∞-norm error bounds, computed on a $s = 20$ input-projected system, are represented on (b) by solid lines.

good illustration of the effect of input projection on the performance of the models.

First, let us examine the evolution of the 2-norm error of the balanced and observable models in Figure 5(a). When increasing the size of the models, the relative error is observed to decrease much faster for the balanced models than for the observable ones. Note that some points of the observable models are missing which means that their associated relative error considerably exceeds 100%. Notably, owing to the input projection, a limit of accuracy is reached by the balanced models as their size r is increased. Indeed, the 2-norm error between the original impulse response $\mathsf{G}(\omega)$ and that of an input-projected system $\widetilde{\mathsf{G}}(\omega)$ of rank s, which was given in Eq. (2.14), can also be expressed as a function of the observable eigenvalues λ_j by

$$||\mathsf{G}-\widetilde{\mathsf{G}}||_2^2=\sum_{j=s+1}^{n}\lambda_j. \tag{4.2}$$

The resulting relative errors have been plotted in Figure 5(a) by dots as a function of the input projection rank s. In other words, for an input projection of rank s, the associated dot yields the limit of accuracy of the corresponding balanced model. This statement is illustrated by dashed lines which account for the error associated with the input projections of rank $s=4,10,16,20$. Note that the observable eigenvalues can be directly used to compute the limit of accuracy of the balanced models. Interestingly, provided that the limit is not reached, the performance of the balanced models is the same whatever the model size r. This observation is consistent with our previous results where we have shown that the first s HSVs and balanced modes are converged when using an input projection of rank s. Consequently, our procedure closely approximates the exact balanced truncation on the original system (without input projection) until the limit of accuracy due to the projection is reached. Increasing the rank of input projection then delays this limit.

Examining the evolution of the relative ∞-norm error in Figure 5(b), the same conclusions arise. Yet, it is interesting to consider this norm because of the availability of theoretical bounds on the discrepancy between the approximate and exact transfer functions in the case of the balanced models. The transfer function $\widetilde{\mathsf{G}}_r$ of the ROM approximates that of the input projected system $\widetilde{\mathsf{G}}$ while guaranteeing[23] the relation

$$\sigma_{r+1}<||\widetilde{\mathsf{G}}-\widetilde{\mathsf{G}}_r||_\infty\le 2\sum_{j=r+1}^{n}\sigma_j, \tag{4.3}$$

based on the associated HSVs σ_j. The lower bound is valid for any ROM, whereas the upper bound is valid for models based on balanced truncation. Assuming the HSVs decrease rapidly, as in the present flow configuration, the upper bound is close to the lower bound achievable by any reduced-order model and the procedure is said to be quasi-optimal. Considering the convergence of the HSVs previously mentioned, it is reasonable to consider these bounds as approximate bounds on $||\mathsf{G}-\widetilde{\mathsf{G}}_r||_\infty$. The representation of the associated relative errors is depicted in Figure 5(b) by solid lines. As these bounds are converged for ROMs of small size (in terms of input projection rank s), the error of the balanced models is observed to lie between these bounds until the limit of accuracy is reached. Note that these error bounds are computed from the HSVs of a $s=20$ input-projected system. Interestingly, the performance of the balanced models is very close to the lower bound achievable by any ROM.

We conclude that both models succeed in capturing the full input-output behavior of the original system. Observable models are clearly outperformed by balanced models. In addition, the performances of the balanced models are quasi-optimal and subject to theoretical bounds, while those of observable models are not.

D. Frequency response

In the case of a multiple input multiple output (MIMO) system, a standard way of quantifying the synthesized frequency response is to compute the maximum singular value of the transfer function. For the full system, it is simply computed by the norm introduced in Sec. II A 2 by $||\mathsf{G}^\dagger(\omega)||=\sqrt{\mathsf{G}(\omega)\mathsf{G}^\dagger(\omega)}$. For a ROM of size r, it is computed similarly by using the corresponding transfer function $\widetilde{\mathsf{G}}_r(\omega)$ (see Appendix B3).

The representation of this quantity, see Figure 6, is known as the singular value Bode plot. We have depicted in Figures 6(a)–6(c) the frequency responses of the balanced and observable models of size 10, 20, and 30, respectively. Note that the balanced models are based on balanced modes computed for an input projection rank $s=20$. The exact frequency response clearly highlights a preferred frequency around $\omega=0.79$ which corresponds to the amplification of

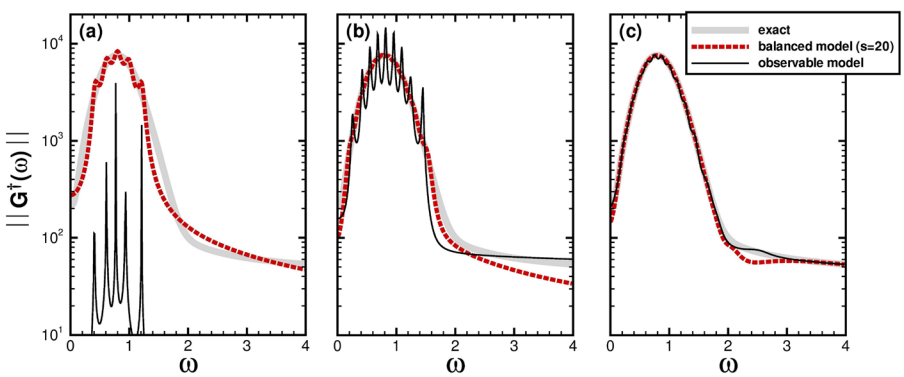

FIG. 6. (Color online) Singular value Bode plot of the full system compared to those of balanced and observable models. Figures (a)–(c) account for ROMs of size 10, 20, and 30, respectively. The balanced models are computed on a $s=20$ input-projected system.

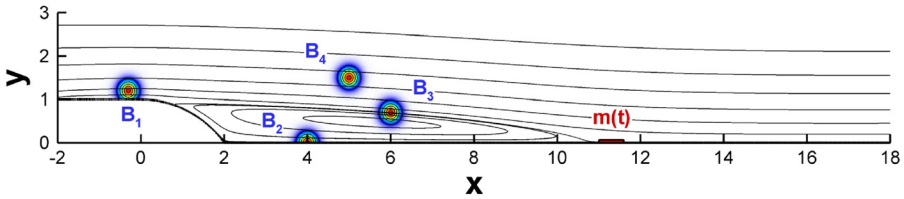

FIG. 7. (Color online) Representation of the four chosen inputs by their vertical component. The streamlines of the base flow and the position of the sensor are also displayed.

perturbations through the shear layer due to the Kelvin-Helmholtz instability. These plots are a clear demonstration of the superiority of the balanced models in capturing the dynamics of the system. We see that even a balanced model of size 10 roughly approximates the original response, while a 20 sized model yields a very good approximation of the frequential response peak. Meanwhile, observable models are completely unable to recover the most important trend of the input-output behavior for these sizes. Observable models eventually capture the exact transfer function for models of size higher than approximately 30, see Figure 6(c).

E. Modeling the dynamics of some localized actuators

In this last part, we illustrate the ability of the ROMs to capture the dynamics from any input to the sensor. To this end, we arbitrarily choose four actuators in the upstream part of the flow and investigate their impulse response on the sensor. Their spatial distribution, denoted by B_1, B_2, B_3, and B_4, are chosen of Gaussian shape on the vertical momentum component, see Figure 7. These Gaussians have a width (full width at half maximum) of 0.4, a height of 1, and are centered at $(-0.3;\ 1.2)$, $(4;\ 0)$, $(6;\ 0.7)$, and $(5;\ 1.5)$, respectively.

Impulse responses of the full system are computed by time-stepper simulations of the linearized Navier-Stokes equations by taking these inputs as initial conditions, namely $\mathsf{X}(t=0)=B_i$ for $i=[1;\ 4]$. Impulse responses of the ROMs are also considered, they are directly computed by $\mathsf{C}_r e^{\mathsf{A}_r t}\mathsf{S}^{\dagger}\mathsf{B}_i$. Both are represented in Figures 8(a)–8(d) for the four inputs. The balanced and observable models have a size $r=20$ and the balanced model was designed from an input projection of rank $s=20$. As expected, we observe that the response from all the inputs investigated here is accurately captured by the balanced model. Meanwhile, the observable model is clearly not as efficient at modeling the main pulses and even sustains undesired oscillations at larger times.

These results are consistent with our previous observations shown in Figures 5 and 6 since the balanced model has already a low error for a size $r=20$ which is not the case for the observable model. These examples illustrate the ability of the ROMs to represent the dynamics of localized inputs that do not intervene in the model reduction process but also the superiority of the balanced models to reach this goal.

V. CRITICAL ASSESSMENT

The results obtained in the present study illustrate the efficiency of the ROMs in capturing the original transfer function. However, the flow configuration considered here is relatively simple; the dynamics are two-dimensional, and there is only one sensor. Thus, we raise questions regarding the applicability of input projection in realistic flows.

Let us first describe a situation where the present techniques are readily usable to design a low-order closed-loop controller. A flat plate boundary layer is subject to two-dimensional instabilities (Tollmien-Schlichting (TS) waves). We need one upstream sensor for the estimation (just upstream of branch I), one actuator (near branch I), and one sensor for the control objective (near branch II). If the noise triggering the transition is unknown (which is usually the case), then a ROM describing the dynamics from the whole input space and the actuator to the two sensors is required. Hence, the input projection technique applied with two

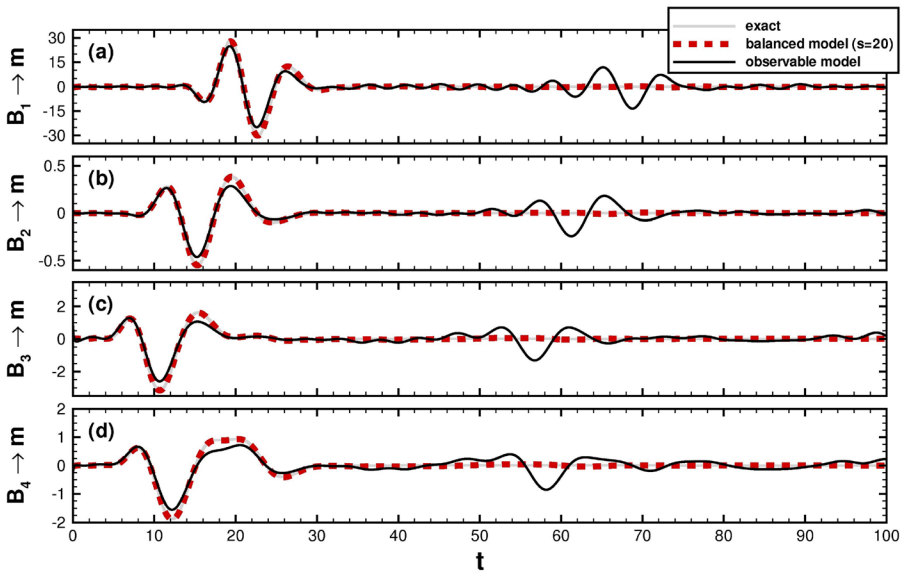

FIG. 8. (Color online) Figures (a)-(d) represent the impulse responses of the four different inputs. The exact solutions come from direct numerical simulations where the number of degrees of freedom is about $n \approx 360\ 000$. The dashed and solid lines account for balanced and observable models of size 20, respectively. Note that the balanced model has been computed with an input projection of rank $s=20$.

sensors should be effective for this purpose. Note that Bagheri *et al.*[2] assume that the upstream noise is known, which is unphysical in some sense. Also, in the control objective, we only require the measurement at the downstream sensor to be reduced, not the whole perturbation energy. Indeed, this would have required the output projection technique, which is not tractable here since the number of inputs is too high.

As soon as considering three-dimensional perturbations or when increasing the Reynolds number, the flow dynamics may become much more complex. In addition, a larger number of sensors may be required to accurately estimate the flow.[4] In these cases, the use of input projection raises some practical issues.

First, the present techniques still hold for three-dimensional flows but with three-dimensional operators and discretizations. Since the resulting dynamical systems are much bigger, iterative techniques rather than direct inversion techniques are required to compute the snapshots. For example, one could use the temporal expressions of the Gramians and solve the direct and adjoint linearized Navier-Stokes equations to compute the snapshots and approximate the Gramians.[4]

Second, the number of direct and adjoint simulations may be much larger. Indeed, one adjoint simulation is required for each additional sensor. Furthermore, the flow dynamics may be significantly more complex so that it may not be represented by as few number of degrees of freedom as in the numerical example exposed here. As a result, we expect that more observable modes (i.e., additional direct simulations) would be required for an accurate input projection. In addition, the singular value decompositions of the matrices $\mathbf{Y}^{\dagger}\mathbf{Y}$ and $\mathbf{Y}^{\dagger}\mathbf{X}$ may even become challenging. For these reasons, the possibly large number of sensors and of required observable modes clearly constitutes the bottleneck of the input projection procedure.

Lastly, the model reduction of more complex dynamics would result in a slower fall-off of the observable eigenvalues and HSVs. Consequently, more observable and balanced modes would be required to design efficient ROMs. In particular, these ROMs may be too large to be used in the design of real-time closed-loop controllers. However, one has to keep in mind that the input projection technique is quasi-optimal in capturing the dynamics from unknown forcing and no other technique would perform better.

We voluntarily considered in this work all the degrees of freedom as inputs in view of designing ROMs which are robust with respect to uncertainties on the noise. Thus, if the input projection procedure fails to design sufficiently low-order models, then the alternative solution would be to gain insight into the particular flow physics. For instance, one may resort to experimental investigations or to receptivity analyses to gain additional information on the noise that one desires to reproduce.

VI. CONCLUSION

In this article, we have described how to approximate balanced truncation for large linear systems when the number of inputs is large. The procedure has been derived on the two-dimensional Navier-Stokes equations subject to an unknown noise (the inputs) and with a single sensor (the output). We introduced a technique called input projection which consists of projecting the input space onto a low-dimensional subspace while optimally preserving the original transfer function. The optimal projection appears as the orthogonal projection onto the most observable modes, namely the leading eigenvectors of the observability Gramian. Connections with the already existing output projection technique introduced by Rowley[23] are also highlighted.

The whole procedure is applied to a stable linear system: the flow over a rounded backward-facing step. A time-dependent forcing term, viewed as a noise, is assumed to act equally on each degree of freedom of the flow state while the sensor is placed near the reattachment point. As a first step, the most observable modes are computed and seen to extend in the upstream part of the flow. Then, the balanced modes of the input-projected systems are computed and observed to converge when increasing the rank of input projection. Reduced-order models are obtained by projecting the input-projected systems onto the leading balanced and observable modes. These ROMs are evaluated by examining their synthesized frequency response. For both projection bases, the frequency selection process of the original system is recovered as we accurately model the frequency response peak associated with the Kelvin-Helmholtz instability. To quantify this performance, the 2-norm and ∞-norm of the error between the reduced and exact transfer functions were computed. We found that the balanced models have an error fall-off that decreases quickly until a limit fixed by the rank of input projection. Mostly, the performances of the balanced models are subject to theoretical bounds and observed to be quasi-optimal. On the other hand, observable models are suboptimal in fulfilling the same objective and do not yield any theoretical bounds on this error. Nevertheless, it is observed to tend to zero when increasing the size of the models. A better efficiency of the balanced models to reach a desired accuracy is clearly identified, which is consistent with the existing literature.

In summary, the balanced truncation of input-projected systems has been shown to yield efficient ROMs which capture the dynamics from any input to a given output. This technique is (i) quasi-optimal in achieving this goal and (ii) subject to theoretical bounds. This contribution may be a promising tool in view of designing reduced models of systems where only a few flow measurements are available while the position of the forcing is unknown. Therefore, it may be a useful addition to the tools of modern flow control theory to design real-time closed-loop controllers.

ACKNOWLEDGMENTS

The authors gratefully acknowledge the French "Délégation Générale pour l'Armement" (DGA) for financial support.

APPENDIX A: EXPRESSING THE LINEARIZED NAVIER-STOKES EQUATIONS AS AN INPUT-OUTPUT STATE-SPACE SYSTEM

Considering a numerical approach, we proceed by discretizing equations (2.2). The system may be written in a finite-sized matrix form as

$$\begin{pmatrix} \mathsf{Q}_1 & 0 \\ 0 & 0 \end{pmatrix} \frac{d}{dt} \begin{pmatrix} \mathsf{X}_1 \\ \mathsf{X}_2 \end{pmatrix} = \begin{pmatrix} \mathsf{A}_1 & \mathsf{A}_2^* \\ \mathsf{A}_2 & 0 \end{pmatrix} \begin{pmatrix} \mathsf{X}_1 \\ \mathsf{X}_2 \end{pmatrix} + \begin{pmatrix} \mathsf{Q}_1 & 0 \\ 0 & 0 \end{pmatrix} \begin{pmatrix} \eta(t) \\ 0 \end{pmatrix}, \tag{A1a}$$

$$m(t) = \begin{pmatrix} \mathsf{C}_1 & 0 \end{pmatrix} \begin{pmatrix} \mathsf{X}_1 \\ \mathsf{X}_2 \end{pmatrix}, \tag{A1b}$$

where X_1 denotes the velocity field and X_2 represents the corresponding pressure field. The linearized Navier-Stokes operator has been decomposed so that A_1 accounts for the convection and diffusion, while A_2 and A_2^* are the parts relative to the incompressibility and pressure effects, respectively. Q_1 is the mass matrix, it also stands for the inner product associated with the kinetic energy of perturbations, namely $\mathsf{X}_1^* \mathsf{Q}_1 \mathsf{X}_1 = \int_\Omega \boldsymbol{u}^2 \, d\Omega$, where Ω is the fluid volume. $(\mathsf{C}_1,0)$ denotes the vector of the discretized sensing $\mathcal{C}$ operator.

To reformulate the above Eq. (A1) into a standard state-space form, we restrict the system state to its divergence-free velocity field.[27] We first multiply the momentum equation by $\mathsf{A}_2 \mathsf{Q}_1^{-1}$, which yields, assuming that $\mathsf{A}_2 \dot{\mathsf{X}}_1 = 0$, an expression for the pressure in terms of the velocity field

$$\mathsf{X}_2 = -\left(\mathsf{A}_2 \mathsf{Q}_1^{-1} \mathsf{A}_2^*\right)^{-1} \left[\left(\mathsf{A}_2 \mathsf{Q}_1^{-1} \mathsf{A}_1\right) \mathsf{X}_1 + \mathsf{A}_2 \eta(t)\right]. \tag{A2}$$

We can then eliminate the explicit divergence constraint to write the equations in the desired form

$$\frac{d\mathsf{X}_1}{dt} = \mathsf{P}_1 \mathsf{A}_1 \mathsf{X}_1 + \mathsf{P}_1 \mathsf{Q}_1 \eta(t), \tag{A3a}$$

$$m = \mathsf{C}_1 \mathsf{X}_1, \tag{A3b}$$

where we have introduced the matrix P_1 defined by

$$\mathsf{P}_1 \mathsf{Q}_1 = \mathsf{I} - \mathsf{Q}_1^{-1} \mathsf{A}_2^* \left(\mathsf{A}_2 \mathsf{Q}_1^{-1} \mathsf{A}_2^*\right)^{-1} \mathsf{A}_2. \tag{A4}$$

Notably, $\mathsf{P}_1 \mathsf{Q}_1$ reduces to the projection matrix onto the divergence-free space and P_1 is a Hermitian operator $\left(\mathsf{P}_1^* = \mathsf{P}_1\right)$. Since we assumed that $\eta(t)$ is a divergence-free state, we have $\mathsf{P}_1 \mathsf{Q}_1 \eta(t) = \eta(t)$. Finally, by defining $\mathsf{A} = \mathsf{P}_1 \mathsf{A}_1$ and $\mathsf{C} = \mathsf{C}_1$, we recover Eq. (2.3)

$$\frac{d\mathsf{X}}{dt} = \mathsf{A}\mathsf{X} + \eta(t), \tag{A5a}$$

$$m(t) = \mathsf{C}\mathsf{X}. \tag{A5b}$$

APPENDIX B: INTRODUCING THE INNER PRODUCTS IN THE DISCRETIZED EQUATIONS

Adjoint operators denoted by the superscript † are different in general from the standard transconjugate *. We chose the inner product associated with the kinetic energy for both the states and the inputs, namely $\langle \mathsf{Z}_1, \mathsf{Z}_2 \rangle = \mathsf{Z}_1^* \mathsf{Q}_1 \mathsf{Z}_2$ for all states or inputs Z_1 and Z_2. As a result, the mass matrix Q_1 intervenes in the definition of the adjoint operators.

Considering the definition of $\mathsf{A}^\dagger$ and $\mathsf{C}^\dagger$ introduced in Sec. II A 2, it is easily found that $\mathsf{A}^\dagger = \mathsf{Q}_1^{-1} \mathsf{A}^* \mathsf{Q}_1$ and $\mathsf{C}^\dagger = \mathsf{Q}_1^{-1} \mathsf{C}^*$. The operator $\mathsf{P}_s = \mathsf{R}\mathsf{R}^\dagger$ has been introduced as the orthogonal projection onto the first s observable modes acting on any flow state or input. Analogously, considering our choice of inner product, it can be expressed as $\mathsf{P}_s = \mathsf{R}\mathsf{R}^* \mathsf{Q}_1$, so that $\mathsf{R}^\dagger = \mathsf{R}^* \mathsf{Q}_1$.

1. Observability Gramian

Observable modes are the eigenvectors associated with the largest eigenvalues of the observability Gramian

$$\mathsf{G}_o = \frac{1}{2\pi} \int_{-\infty}^{+\infty} \left(-j\omega \mathsf{I} - \mathsf{A}^\dagger\right)^{-1} \mathsf{C}^\dagger \mathsf{C} \left(j\omega \mathsf{I} - \mathsf{A}\right)^{-1} d\omega. \tag{B1}$$

Replacing the adjoint quantities by their explicit expression, the observability Gramian may be written as

$$\mathsf{G}_o = \mathsf{Q}_1^{-1} \left(\frac{1}{2\pi} \int_{-\infty}^{+\infty} \left(-j\omega \mathsf{I} - \mathsf{A}^*\right)^{-1} \mathsf{C}^* \mathsf{C} \left(j\omega \mathsf{I} - \mathsf{A}\right)^{-1} d\omega \right), \tag{B2}$$

and the flow states $\widehat{\mathsf{Y}}(\omega)$ introduced in Sec. III B are then defined by $\mathsf{Q}_1 \widehat{\mathsf{Y}}(\omega) = \left(-j\omega \mathsf{I} - \mathsf{A}^*\right)^{-1} \mathsf{C}^*$. Finally, the procedure outlined in Sec. II to compute the observable modes can be performed by replacing $\widehat{\mathsf{Y}}^\dagger(\omega)$ by $\widehat{\mathsf{Y}}^*(\omega) \mathsf{Q}_1$. The observability Gramian then reads $\mathsf{G}_o \approx \mathbf{Y}\mathbf{Y}^* \mathsf{Q}_1$.

2. Controllability Gramian

Let us consider the controllability Gramian of the input-projected system

$$\mathsf{G}_c = \frac{1}{2\pi} \int_{-\infty}^{+\infty} \left(j\omega \mathsf{I} - \mathsf{A}\right)^{-1} \mathsf{R}\mathsf{R}^\dagger \left(-j\omega \mathsf{I} - \mathsf{A}^\dagger\right)^{-1} d\omega. \tag{B3}$$

Making explicit the adjoint operators, we obtain the new expression

$$\mathsf{G}_c = \left(\frac{1}{2\pi} \int_{-\infty}^{+\infty} \left(j\omega \mathsf{I} - \mathsf{A}\right)^{-1} \mathsf{R}\mathsf{R}^* \left(-j\omega \mathsf{I} - \mathsf{A}^*\right)^{-1} d\omega \right) \mathsf{Q}_1. \tag{B4}$$

The input projection procedure previously introduced in Sec. II can then be derived by using the states $\widehat{\mathsf{X}}(\omega) = \left(j\omega \mathsf{I} - \mathsf{A}\right)^{-1} \mathsf{R}$ and its adjoint $\widehat{\mathsf{X}}^\dagger(\omega) = \widehat{\mathsf{X}}^*(\omega) \mathsf{Q}_1$. The resulting factored form of the controllability Gramian can be written as $\mathsf{G}_c \approx \mathbf{X}\mathbf{X}^* \mathsf{Q}_1$.

3. Generalized transfer functions

We see in this appendix how to compute the transfer functions and their associated norms. First, let us consider the full transfer function of system (2.3). It is defined by

$$\mathsf{G}(\omega) = \mathsf{C} \left(i\omega \mathsf{I} - \mathsf{A}\right)^{-1}, \tag{B5}$$

which is a vector of size $1 \times n$. $\mathsf{G}(\omega)$ can also be expressed as a function of the flow states $\widehat{\mathsf{Y}}(\omega)$ by

$$\mathsf{G}(\omega) = \widehat{\mathsf{Y}}^{\dagger}(\omega) = \widehat{\mathsf{Y}}^{*}(\omega)\mathsf{Q}_1. \tag{B6}$$

The transfer function can be quantified by its associated standard 2-norm and ∞-norm[23] given by

$$\begin{aligned} ||\mathsf{G}||_2 &= \sqrt{\frac{1}{2\pi}\int_{-\infty}^{+\infty} ||\mathsf{G}^{\dagger}(\omega)||d\omega} \\ ||\mathsf{G}||_{\infty} &= \max_{\omega} ||\mathsf{G}^{\dagger}(\omega)||. \end{aligned} \tag{B7}$$

Practically, we can easily compute these norms from the flow states $\widehat{\mathsf{Y}}(\omega)$ since

$$\begin{aligned} ||\mathsf{G}^{\dagger}(\omega)|| &= \sqrt{\mathsf{G}(\omega)\mathsf{G}^{\dagger}(\omega)} = \sqrt{\mathsf{G}(\omega)\mathsf{Q}_1^{-1}\mathsf{G}^{*}(\omega)} \\ &= \sqrt{\widehat{\mathsf{Y}}^{*}(\omega)\mathsf{Q}_1\widehat{\mathsf{Y}}(\omega)}. \end{aligned} \tag{B8}$$

Now, we consider the transfer function of the reduced systems obtained from the input projected system (2.13). It has been defined by

$$\widetilde{\mathsf{G}}_r(\omega) = \mathsf{C}_r(i\omega\mathsf{I}_r - \mathsf{A}_r)^{-1}\mathsf{B}_r, \tag{B9}$$

where A_r, B_r, and C_r have been introduced in Sec. II E. The 2-norm and ∞-norm of this transfer function can be computed similarly to that of the full system by replacing $||\mathsf{G}^{\dagger}(\omega)||$ by $||\mathsf{G}_r^{\dagger}(\omega)|| = \sqrt{\mathsf{G}_r(\omega)\mathsf{G}_r^{\dagger}(\omega)}$ in Eq. (B7). The quantity $||\mathsf{G}_r^{\dagger}(\omega)||$ accounts for the synthesized frequency response of the ROMs. It can be computed analogously to that of the full system by replacing $\widehat{\mathsf{Y}}(\omega)$ in Eq. (B8) with its equivalent on the reduced system $\widehat{\mathsf{Y}}_r(\omega)$ which is defined by

$$\widehat{\mathsf{Y}}_r(\omega) = \mathsf{B}_r^{\dagger}(-i\omega\mathsf{I}_r - \mathsf{A}_r^{*})^{-1}\mathsf{C}_r^{*}. \tag{B10}$$

Note that B_r is equal to $\mathsf{S}^{\dagger}\mathsf{R}\mathsf{R}^{\dagger}$ for balanced models and reduces to $\mathsf{R}^{\dagger}$ for observable models. Notably, an equivalent of Eq. (B6) can be expressed for the transfer function of the reduced systems by

$$\widetilde{\mathsf{G}}_r(\omega) = \widehat{\mathsf{Y}}_r^{\dagger}(\omega) = \widehat{\mathsf{Y}}_r^{*}(\omega)\mathsf{Q}_1. \tag{B11}$$

APPENDIX C: LINK WITH OUTPUT PROJECTION

In this appendix, we show that the input projection described in this paper is equivalent to the output projection introduced by Rowley[23] when applied to the adjoint system. First, we consider the adjoint problem associated with Eq. (2.3). It can be written as

$$\frac{d\mathsf{Y}}{dt} = \mathsf{A}^{\dagger}\mathsf{Y} + \mathsf{C}^{\dagger}\upsilon(t), \tag{C1a}$$

$$\zeta(t) = \mathsf{Y}, \tag{C1b}$$

where Y is the adjoint state, $\upsilon(t)$ and $\zeta(t)$ denote the adjoint input and output, respectively. Using the definition of the Gramians previously introduced, one can observe that the controllability Gramian of the direct problem is equal to the observability Gramian of the adjoint one and vice versa. Note that, compared to the direct system, input and output sizes have been exchanged. In particular, the output space of this new system becomes the full state space.

In the output projection method introduced by Rowley,[23] the output dimension is very large and an output projected system is considered. For the present adjoint system, the projection that minimizes the 2-norm error between the original transfer function and the output-projected transfer function is given by the POD of the dataset $\{\mathsf{Y}(t);\, t>0\}$. In other words, it stands for the projection onto the most controllable modes of the adjoint system, or equally to the projection onto the most observable modes of the direct system. As a result, the output projected system can be expressed as a function of the matrix R by

$$\frac{d\mathsf{Y}}{dt} = \mathsf{A}^{\dagger}\mathsf{Y} + \mathsf{C}^{\dagger}\upsilon(t), \tag{C2a}$$

$$\tilde{\zeta}(t) = \mathsf{R}^{\dagger}\mathsf{Y}, \tag{C2b}$$

where we have introduced the low-dimensional projected output $\tilde{\zeta}(t)$. Returning to the direct problem, the input-output system reduces to

$$\frac{d\mathsf{X}}{dt} = \mathsf{A}\mathsf{X} + \mathsf{R}\tilde{\eta}(t), \tag{C3a}$$

$$\tilde{m}(t) = \mathsf{C}\mathsf{X}, \tag{C3b}$$

which governs the dynamics of the input-projected system introduced in Sec. II D.

[1] L. Kaiktsis, G. Karniadakis, and S. Orszag, "Unsteadiness and convective instabilities in two-dimensional flow over a backward-facing step," J. Fluid Mech. **321**, 157 (1996).
[2] S. Bagheri, L. Brandt, and D. S. Henningson, "Input-output analysis, model reduction and control of the flat-plate boundary layer," J. Fluid Mech. **620**, 263 (2009).
[3] S. Bagheri and D. S. Henningson, "Transition delay using control theory," Philos. Trans. R. Soc. London, Ser. A, **369**, 1365 (2011).
[4] O. Semeraro, S. Bagheri, L. Brandt, and D. S. Henningson, "Feedback control of three-dimensional optimal disturbances using reduced-order models," J. Fluid Mech. **677**, 63 (2011).
[5] B. F. Farrell and P. J. Ioannou, "State estimation using a reduced order kalman filter," J. Atmos. Sci. **58**, 3666 (2001).
[6] B. F. Farrell and P. Ioannou, "Accurate low-dimensional approximation of the linear dynamics of fluid flow," J. Atmos. Sci. **58**, 2771 (2001).
[7] B. Moore, "Principal component analysis in linear systems: Controllability, observability, and model reduction," IEEE Trans. Autom. Control **26**, 17 (1981).
[8] G. E. Dullerud and F. Paganini, "A course in robust control theory: A convex approach," in *Texts in Applied Mathematics*, Vol. 36 (Springer-Verlag, New York, 2000).
[9] J. B. Burl, *Linear Optimal Control. $\mathcal{H}_2$ and $\mathcal{H}_\infty$ Methods* (Addison Wesley Longman, Inc., Menlo Park, CA, 1999).
[10] T. R. Bewley, "Flow control: New challenges for a new renaissance," Prog. Aerosp. Sci. **37**, 21 (2001).
[11] K. Zhou, G. Salomon, and E. Wu, *Robust and Optimal Control* (Prentice-Hall, New Jersey, 2002).
[12] J. Kim and T. Bewley, "A linear systems approach to flow control," Ann. Rev. Fluid Mech. **39**, 383 (2007).
[13] D. Sipp, O. Marquet, P. Meliga, and A. Barbagallo, "Dynamics and control of global instabilities in open flows: A linearized approach," Appl. Mech. Rev. **63**, 030801 (2010).
[14] J. M. Scherpen, "Balancing for nonlinear systems," Syst. Control. Lett. **21**, 143 (1993).

[15]S. Lall, J. E. Marsden, and S. Glavaski, "A subspace approach to balanced truncation for model reduction of nonlinear control systems," Int. J. Robust Nonlinear Control **12**, 519 (2002).
[16]A. Laub, M. Heath, C. Paige, and R. Ward, "Computation of system balancing transformations and other applications of simultaneous diagonalization algorithms," IEEE Trans. Autom. Control **32**, 115 (1987).
[17]K. Zhou, G. Salomon, and E. Wu, "Balanced realization and model reduction for unstable systems," Int. J. Robust Nonlinear Control **9**, 183 (1999).
[18]T. Kim, "Frequency-domain karhunen-loeve method and its application to linear dynamic systems," AIAA J. **36**, 2117 (1998).
[19]A. C. Antoulas, *Approximation of Large-Scale Dynamical Systems* (SIAM, Philadelphia, 2005).
[20]S. Joshi, J. Speyer, and J. Kim, "A systems theory approach to the feedback stabilization of infinitesimal and finite-amplitude disturbances in plane poiseuille flow," J. Fluid Mech. **332**, 157 (1997).
[21]M. Högberg, T. R. Bewley, and D. S. Henningson, "Linear feedback control and estimation of transition in plane channel flow," J. Fluid Mech. **481**, 149 (2003).
[22]K. Willcox and J. Peraire, "Balanced model reduction via proper orthogonal decomposition," AIAA J. **40**, 2323 (2002).
[23]C. Rowley, "Model reduction for fluids using balanced proper orthogonal decomposition," Int. J. Bifurcation. Chaos Appl. Sci. Eng. **15**, 997 (2005).
[24]M. Ilak and C. Rowley, "Modeling of transitional channel flow using balanced proper orthogonal decomposition," Phys. Fluids **20**, 034103 (2008).
[25]G. Dergham, D. Sipp, J.-C. Robinet, and A. Barbagallo, "Model reduction for fluids using frequential snapshots," Phys. Fluids **23**, 064101 (2011).
[26]S. Ahuja and C. Rowley, "Low-dimensional models for feedback stabilization of unstable steady states," AIAA Paper No. 2008-553, 46th AIAA Aerospace Sciences Meeting and Exhibit (2008).
[27]A. Barbagallo, D. Sipp, and P. Schmid, "Closed-loop control of an open cavity flow using reduced-order models," J. Fluid Mech. **641**, 1 (2009).
[28]S. Ahuja and C. Rowley, "Feedback control of unstable steady states of flow past a flat plate using reduced-order estimators," J. Fluid Mech. **645**, 447 (2010).
[29]M. Ilak and C. Rowley, "Reduced-order modeling of channel flow using travelling POD and balanced POD," AIAA Paper No. 2006-3194, 3rd AIAA Flow Control Conference (2006).
[30]L. Sirovich, "Turbulence and the dynamics of coherent structures," Q. Appl. Math. **45**, 561 (1987).
[31]C. Rowley, T. Colonius, and R. Murray, "Model reduction for compressible flows using pod and galerkin projection," Physica D **189**, 115 (2004).
[32]T. Duriez, "*Application des générateurs de vortex au contrôle d'écoulements décollés*," Ph.D. thesis (Paris Diderot University, France, 2009).
[33]D. Sipp and A. Lebedev, "Global stability of base and mean flows: a general approach and its applications to cylinder and open cavity flows," J. Fluid Mech. **593**, 333 (2007).
[34]P. R. Amestoy, I. S. Duff, J. Koster, and J.-Y. L'Excellent, "A fully asynchronous multifrontal solver using distributed dynamic scheduling," SIAM J. Matrix Anal. Appl. **23**, 15 (2001).
[35]S. Bagheri, J. Hœpffner, P. J. Schmid, and D. S. Henningson, "Input-output analysis and control design applied to a linear model of spatially developing flows," Appl. Mech. Rev. **62**, 020803 (2009).
[36]K. M. Butler and B. F. Farrell, "Three-dimensional optimal perturbations in viscous shear flow," Phys. Fluids A **4**, 1637 (1992).
[37]J.-M. Chomaz, "Global stabilities in spatially developing flows: non-normality and nonlinearity," Annu. Rev. Fluid Mech. **37**, 357 (2005).
[38]O. Marquet, D. Sipp, J.-M. Chomaz, and L. Jacquin, "Amplifier and resonator dynamics of a low-Reynolds number recirculation bubble in a global framework," J. Fluid Mech. **605**, 429 (2008).